



Selective Laser Hardening of Aluminium AA6061-O Alloy with Nanosecond Laser Pulses

Furat I. Hussein^{1*}, Sanaa Al-Sumaidae² and Ahmed R. Alhamaoy³ Kareem N. Salloomi² and Muhammad Ahmed Obeidi⁴

¹Mechatronics Engineering Department, Al-Khwarizmi College of Engineering, University of Baghdad, Baghdad, 10071 Iraq

²Automated Manufacturing Department, Al-Khwarizmi College of Engineering, University of Baghdad, Baghdad, 10071 Iraq

³Laser and Optoelectronic Eng. Dep., College of Engineering, Al-Nahrain University

⁴School of Mechanical & Manufacturing Engineering, Dublin City University, Dublin, Ireland

ARTICLE INFO

Article history:

Received October 1, 2024

Revised January 24, 2025

Accepted February 10, 2025

Available online March 1, 2025

Keywords:

Nanosecond laser

Al 6061-O alloy

Hardness

Surface Roughness

Laser Hardening

ABSTRACT

Conventional hardening, sometimes, is not economically viable due to consuming additional costs and energy. This makes applying selective hardening on specific regions an attractive alternative for members subjected to local friction and wear. This work is devoted to applying cold working hardening on discrete values on regions of aluminum 6061-O alloy using nanosecond fiber laser of 100 W average power and pulse duration of 81 ns. An exaggerated plasma pressure resulted from ablation a thin coat layer on the metal surface was built in order to cause cold plastic deformation and increase the surface hardness of the alloy. The power density (Pd) and pulse overlap percentage (OV) were employed as working parameters. Due to the sensitivity of aluminium alloys to excessive heating, the criteria of the best outcomes were considered according to the objective of the study in supporting the hardness by strain hardening. The higher attained a significant increase in the hardness associated with less consumed optical energy, the most clean and flawless surface, observed by the high-resolution SEM images, which indicates hardening with cold work. The best hardness value is conducted at a Pd of 4.46 GW/cm² reaching a hardness of 57.6 HV at an OV of 43% and 53.8 VHD at an OV of 77.3%. The X-Ray diffraction analysis (XRD) revealed a reduction of 56% in grain size compared to the original alloy and increase in the number of dislocations density by 378%.

1. Introduction

Aluminium grade 6xxx (Al-Mg-Si) are heat treatable alloys characterized by good corrosion resistance, low density, good strength to weight ratio [1], good coupling of strength and toughness and low cost [2,3]. Strictly speaking, such grade of aluminum alloy produces easily a range of microstructures when subjected to heat treatments [4]. Their excellent weldability and good machinability make them preferable in different applications of industry [5]. All these functions boost demands for such alloys in the

industries of aircraft, automotive, marine, structural members, hydraulic pistons, electrical fittings, bike, and frames, etc. [6-8]. Enhancement of surface hardness can improve some mechanical properties such as wear, tear resistance and fatigue life by imparting residual stresses [8]. The facility of non-contact feature provides simplicity, processing localized regions, and high quality in laser surface hardening, which could make selective laser hardening a solution, especially for complex geometries [10,11]. Hardening can be done in

* Corresponding author.

E-mail address: furatnejjar@uobaghdad.edu.iq

DOI: [10.24237/djes.2025.18107](https://doi.org/10.24237/djes.2025.18107)

This work is licensed under a [Creative Commons Attribution 4.0 International License](https://creativecommons.org/licenses/by/4.0/).



two routes, either thermally through heating and quenching at a certain cooling rate to introduce new phases in the microstructure [11-13] or by imparting residual stresses at the surface and below to a certain depth. The latter process involves ablation of a thin coat on the surface of the metal by short laser pulses. This generates an exaggerated plasma pressure capable of introducing cold working through generating enough density of dislocations, twinning, residual stresses and compressive residual stresses [14,15].

Shortening the pulse width leads to fewer thermal effects during the interaction of the laser with matter due to decreasing the interaction time regarding electron cooling and lattice heating times [16]. Although nanosecond pulses are much shorter than milliseconds, the nature of the interaction is still associated with greater thermal effects compared to employing shorter pulses such as femtosecond and picosecond pulses [17]. Irradiation of a metal surface with nanosecond pulses results in sequential processes due to interaction between laser beam and matter [18]. Surface temperature rise followed with melting, vaporization, plasma formation and shockwaves are the fundamental processes to achieve material removal via ablation [19]. This may yield side effects such as heat affected zone (HAZ), micro cracks, recast layer, surface roughening and extruded flakes. However, processing with nanosecond pulses yield significantly fewer thermal effects at the substrate compared with the microsecond and millisecond pulses [14,18]. Ablation with nanosecond pulses is a thermal process in nature and it may introduce metallurgical phase change in the target metal as well as pressure waves creating in residual stresses at the end of the process [21]. Covering the base metal with an absorbent layer, such as a polymer or sprayed coat switches the interaction between the laser and coated layer rather than the underlying metal itself. The high power density of the laser ablates and vaporizes the layer and ionizes the atoms forming a plasma plume of enough pressure to do plastic deformation on the metal. Confining the interaction and plasma plume with a window such as a water layer

significantly magnify the induced pressure and deformation at the target [20,21].

Many researches showed that processing metals surfaces with nanosecond laser pulses can contribute in reinforcing the surface hardness in expense on morphology degradation. O. Netprasert et al. [24] experimentally investigated the effect of average power, speed and pulse overlap on the surface hardening for AISI 420 stainless using nanosecond pulse fiber laser. The optimum parameters resulted in an increase in surface hardness to 250% over a depth of 60-80 μm with no melting or surface damage noticed after the process. M. Ezzat et al. [25] employed pulsed nanosecond Nd: YAG laser in treating an aluminum alloy grade 1100 to enhance surface hardness associated with studying surface morphology. The peak value for Vickers microhardness was recorded before the laser intensity exceeded 750.16 MW/cm^2 where a drop in value begins. A. Mostafa et al. [26] studied the feasibility of using two wavelengths for a nanosecond Nd:YAG; 1064 nm and its second harmonic generation 532 nm in increasing the hardness of an aluminium alloy grade 7075. Without coating on the metal surface, a direct proportionality was found between the energy density and the number of shots per unit area with the hardness which reached its maximum value of 80 HV. A. Kadhim et al. [27] deduced that the laser pulse energy has a direct relationship with surface microhardness for aluminium alloy grade 2024-T3 when coated with paint and irradiated with nanosecond laser pulses. They found that the impact of shockwaves due to applying laser pulses has a direct relationship with the surface hardness. Increasing the pulse energy of one Joule would increase the microhardness by 4.8 times than before treatment, degrade the surface roughness from 0.5 to 1.55 μm and decrease the wear rate to 34%.

The work aims to elect an best value of hardness associated with a minimum value of degradation in the surface quality represented by the less microroughness and thermal defects for 6061 aluminium alloys. The combination of the nanosecond laser as a precise tool and CAD features gives the facility of hardening selected

discrete regions on metal surfaces to apply surface hardening. The process was applied using high speed fiber nanosecond laser to investigate the impact of nanosecond pulses on the surface in the creation of dislocations and residual stresses which contribute to the increase in surface hardness. The highest value of surface hardness is not the only criterion, it should be associated with a surface of acceptable roughness and no or less thermal defects such as voids, microcracks, and recast ejected molten metal. It is worth mentioning that these could be attained when the interaction is done with the polymeric coat only, not with the base Al metal and this could be achieved through investigating the optimum working parameters.

2. Experimental

2.1 Samples preparation

An aluminum alloy grade 6061-O of 1.6 mm thickness, was employed in the current investigation. The chemical composition of the alloy analysis was performed through the XRF technique and tabulated in Table 1. Vickers hardness (VHD) and roughness tests were applied to the raw sample of the alloy. the roughness (Ra) was taken in two directions along the laser spot motion vector (Rax) and normal to the vector (Ray) as presented in Table 2.

The samples were cut as square shapes of side length 76 mm and then cleaned with distilled water and ethanol. After that, they were coated with a thin layer of black paint for two purposes: to ablate and build a plasma plume of specific pressure, as well as to shield the base metal from excessive heating and direct contact with the laser.

Table 1: The chemical composition of employed aluminium 6061-O alloy

	Si %	Fe %	Cu %	Mn %	Mg %	Cr %	Zn %	Ti %	others %	Al %
Test values	0.571	0.411	0.187	0.091	0.801	0.20	0.010	0.062	0.015	97.7
Standard [28]	0.4-0.8	0.0-0.7	0.15-0.40	0.0-0.15	0.8-1.2	0.04-0.35	0.0-0.25	0.0-0.25	---	95.85-98.56

Table 2: The microhardness and surface roughness for employed aluminium 6061-O alloy

Vickers Hardness VHD (HV)		32
Surface Roughness Ra (µm)	Rax	0.549
	Ray	0.688

2.2 Samples processing

A single-mode Q-switched fiber laser from Wuxi Raycus Fiber Laser Technologies Co., LTD. / China, Model WXRFL that operates at the fundamental wavelength of 1064 ± 4 nm has been utilized in the hardening process of the raw aluminum samples. The laser system has an average power of 100W, 81 ns pulse duration, and a frequency range of pulses from 10 to 100 kHz. The laser system is equipped with a focusing lens of 12.5 mm focal length and an x-y Galvo scanner to direct the laser beam over the working plane with a maximum high speed of 6000 mm/s.

Each cut squared sample, of 76 mm side length, is divided into 36 zones of 8×8 mm side length for irradiation, each zone was processed with a different set of working parameters as shown in Figure 1a. Each sample was treated by immersing it in deionized water to a depth of 3 mm beneath the water's surface. Figure 1b illustrates a schematic for the setup where the laser beam is focused on the coat surface to achieve ablation. The laser spot covers the working area during the hardening process by scanning the area with multiple passes of hatch spacing (H) of 10%. Another overlap is done between sequential laser pulses (OV) along the scanning speed vector of a variable value

depending on the scanning speed, laser spot diameter, and the frequency of pulses.

2.3 Working parameters

Three working parameters were employed in this investigation to process 36 zones on each cut-squared sample, with three cut samples the total number of processed zones became 108. Employing an identical set of working parameters, every zone was repeated three times

to obtain an average value for each requested outcome. Laser beam power density, the frequency of pulses, and the overlapping ratio between laser pulses are the three investigated parameters. The power density was varied through changing the spot diameter or pulse frequency while the overlap ratio varied by manipulating the frequency of pulses and scanning speed which taken out according to the following relations [29]:

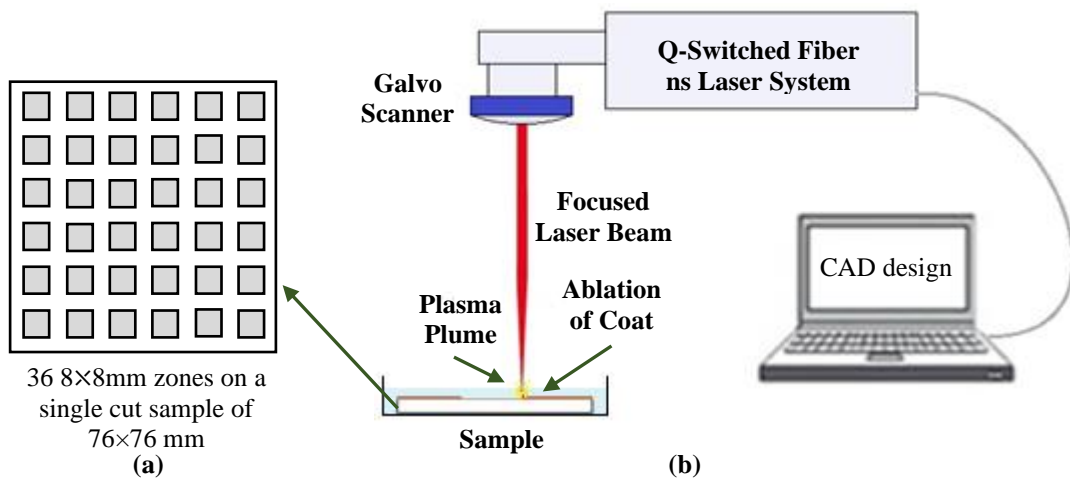


Figure 1. (a) 36 different selectively processed zones with different sets of parameters, (b) The experimental setup (not in scale)

$$Pd = \frac{4P_{av}}{\pi f \tau D^2} \quad (1)$$

$$OV = 1 - \frac{v}{Df} \quad (2)$$

where P_{av} is the average power (W), f is the frequency of pulses (Hz), τ is the pulse duration (ns), D is the spot diameter (mm), and v is the scanning speed (mm/s).

Experiments were done through investigation of the effect of each single parameter variation on the surface hardness and resulting roughness. Every input parameter under study was varied over a defined range of values while keeping the others constant, which yields a set of data servers the intended goals. This procedure was repeated three times by varying each parameter considered to be of interest and thus obtaining a family of important data for that purpose. Table 3 tabulates the minimum and maximum limits of utilized working parameters. The experiments are

designed based on one factor at a time method for the range of each factor with a regular increase ensuring changeable variation in the outcome of interest. This route can ensure an in-depth exploration of each individual effect on the surface hardness and side effects of processing.

Table 3: The minimum and maximum limits of working parameters ranges.

Parameter	Units	Minimum limit	Maximum limit
Frequency (f)	kHz	20	25
Power density (Pd)	GW/cm ²	3.39	19.65
Overlap ratio (OV)	%	-12	80

2.4 Experimental tests

Evaluation of the microhardness values was applied through many Vickers hardness tests using a Digital Micro-hardness tester (Q-Time,

TH-715) (China). Measurement of surface roughness, arithmetic mean roughness Ra, was applied in two directions; along and normal to the velocity vector in the x-direction (Rax) and y-direction (Ray) respectively. The test was carried out through a roughness tester AR-132C (China). Scanning electron microscope type Axia ChemiSEM from Thermo Fisher Scientific Inc was utilized to observe the surface condition of samples and investigate the surface alterations after the hardening.

The microstructural characteristics of the metal before and after surface processing were compared and evaluated using X-ray diffraction (XRD) analysis using a Shimadzu diffractometer. The measured width of the diffracted peaks at full-width half maximum (FWHM) provides insight into crystallographic information and structural analysis utilizing the Williamson-Hall method [23]:

$$\beta \cos \theta = \frac{K\lambda}{D} + 4\epsilon \sin \theta \quad (3)$$

where β is FWHM (rad), K is a constant depending on the crystallite size, λ is the x-ray wavelength (0.15406 nm), D is the crystallite size, θ is the Bragg angle (rad) and ϵ is the induced strain.

The slope and intercept of the linear plot between the terms $\beta \cos \theta$ versus $4 \sin \theta$ give information about the microstrain (ϵ) and grain size ($K\lambda/D$) respectively.

The broadening of the diffraction peak is related to the changes in grain size as in the Scherrer equation [30]:

$$D = \frac{K\lambda}{\beta \cos \theta} \quad (4)$$

D is related directly to the dislocation density through [31]:

$$\rho = \frac{1}{D^2} \quad (5)$$

The extent of residual stresses was calculated from the XRD test using $\sin^2\Psi$ method where ψ is an angle that describes the orientation of the sample with the diffraction vector. The slope of the line in the d spacing - $\sin^2\Psi$ plot was used in analyzing the extent of

residual stresses according to the following relation [32]:

$$\sigma_r = \frac{m}{d} \left(\frac{E}{1 + \nu_p} \right) \quad (6)$$

where σ_r is the induced residual stresses, m is the slope of the $d - \sin^2\Psi$ plot, E is the modulus of elasticity, and ν_p is the Poisson's ratio of the material.

3. Results and discussion

3.1 Microhardness

Laser hardening was carried out by processing several sample groups that were classified based on different sets of parameters. Each sample gave a distinct value of hardness which yielded diverse output of results. It was found that the OV had a significant effect on the obtained microhardness. The effect of varying OV on the microhardness was studied at three classified levels of Pd domains; low level ranges from 3.93 to 4.91 GW/cm², moderate level from 6.98 to 8.73 GW/cm² and high level from 15.72 to 19.65 GW/cm². Figure 2 shows the impact of OV on the microhardness (VHD) values along the low-level range of power densities where all curves exhibit the same behavior. These experiments applied with a spot diameter of 0.04 mm, range of frequencies from 20 to 25 kHz, and range of scanning speeds from 200 to 500 mm/s. The microhardness exhibits considerable variations horizontally along the range of OV variance and vertically by switching between different values of Pd's. The maximum values of hardness can be noticed at the highest scanning speeds where the OV between pulses is the minimum. Decreasing the speeds leads to an increase in the OV accompanied by a reduction in the hardness. When the scanning speed drops more, the increase in the percentage of OV yielded ascending in the hardness values again giving a flipped Gaussian shape for each curve of power density. The hardness values are magnified as higher Pd levels are utilized to a certain extent. The hardness values exhibit an increasing trend as the Pd switched from 3.39 to 4.09 GW/cm² reaching the peak at 4.46 GW/cm². However, beyond this level, the whole of the curves belonging to the Pd's of 4.46 and

4.68 GW/cm² start decreasing. The largest hardness values are conducted at a Pd of 4.46 GW/cm² reaching a hardness of 57.6 HV at an OV of 43% and 53.8 VHD at an OV of 77.3%.

Although the calculations showed power density values in the giga ranges which are considered extremely high, the behavior of the curve can be justified by the extent of diffused thermal energy inside the target. This can be

determined by the ratio of average laser power to scanning speed to determine the average poured energy per unit area [33]:

$$Ea = \frac{P_{av}}{v D} \tag{7}$$

where Ea is the average energy input (J/cm²).

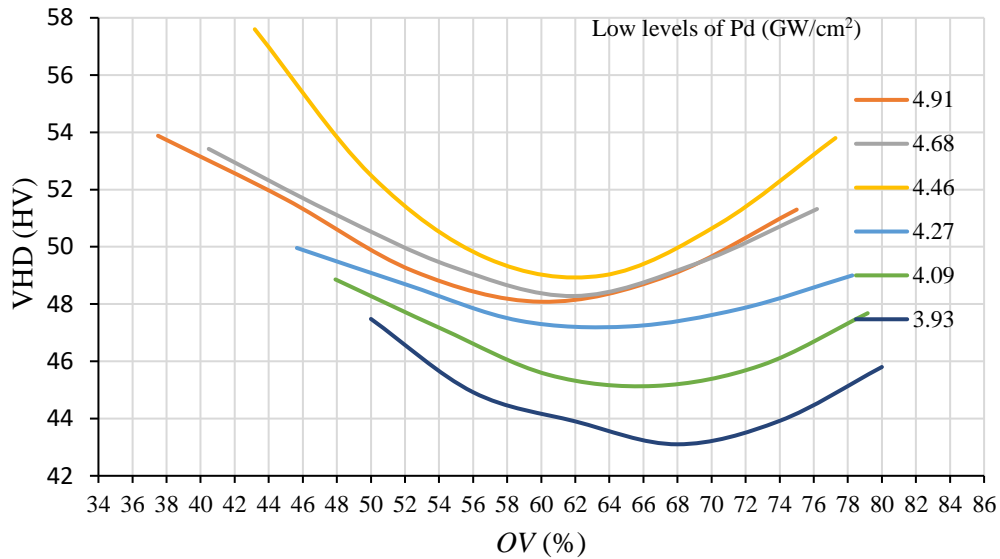


Figure 2. Effects of OV percentage on the surface hardness (VHD) at low levels of Pd ranges from 3.93 to 4.91 GW/cm²

In addition, an increase in the number of pulses in a single position (N) on the surface of a sample devotes poured energy and its thermal side effects on the surface. The number of pulses on a single spot for a given speed and frequency can be expressed as follows [34]:

$$N = \frac{D f}{v} \tag{8}$$

where N is the number of pulses irradiated on a single spot on the sample surface.

Figure 3 shows the impact of increasing Ea and N on the hardness values of the zone that recorded the best hardness values which processed Pd of 4.46 GW/cm², f of 22 kHz, and D of 0.04 mm. The behavior of the curve indicates that the hardening process passes

through two phases; nonthermal, or cold, and thermal. The former is due to the result of the high mechanical pressure which yields cold working that induces residual stresses on the metal surface and beneath. At low values of OV (43%), the Ea is 1.75 kJ/cm², and N is 0.55 pulses/spot, the black coat efficiently ablated. This led to a great build of plasma pressure on the metal surface enough to do cold work and attain a hardening of 57.25 HV. The second phase comes when the scanning speed is lowered which yields increasing in OV , Ea , and an increase in N , the incubation of pulses in a single position, moving the interaction from the cold toward the hot nature. Excessive heating causes heat treatment through heating and subsequent quenching in the metal bulk and the water at room temperature.

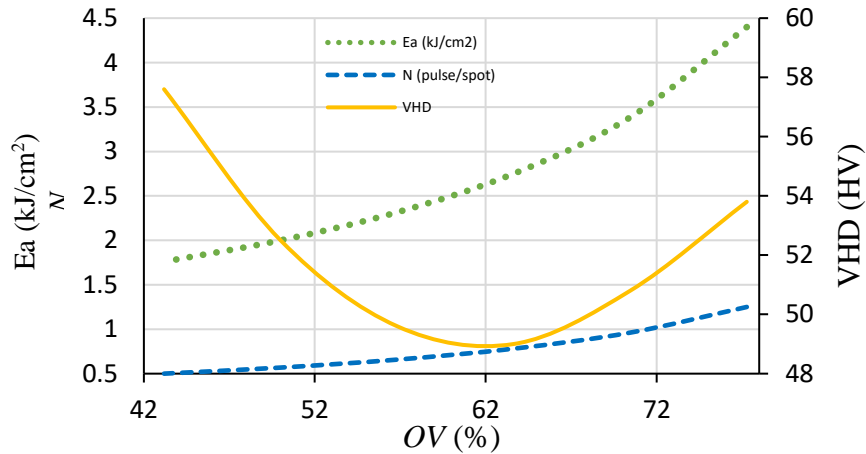


Figure 3. The role of Ea and N on the VHD variation at Pd of 4.46 GW/cm² and f=22 kHz

Returning to Figure 2, switching to different values of Pd's results in the same behavior of curves but diverse values of microhardness. At low levels of Pd, the set of hardness is the lowest, and this rises as the power density increases in its maximum value at Pd of 4.46 where the optimum result was discovered. This can be explained by the plasma pressure that built from the ablation of the black coat which should exceeds the dynamic yield strength [35]:

$$P = \frac{\sqrt{PdATL}}{4} \quad (9)$$

where P is the built pressure (MPa), A is the absorption coefficient of the black coat, T is the transmittance of the window (water) and L is the reduced shock impedance between the metal and the window (kg s/m²).

The strength and mechanical properties of Al 6061-O come from the dislocations and precipitates phases. However, elevating the temperature will lead to a reduction in the presence of these factors resulting in degradation in the yield strength [36]. The hardness of aluminum plate exhibit declines in hardness as the temperature increased from 225°C and up [37].

At power densities higher than 4.46 GW/cm² namely at 4.68 and 4.91 GW/cm², the curves go down traveling to lower values of microhardness accompanied by flattening of the values of hardness at the edges where it was maximum at the optimum value of 4.46 GW/cm².

Minimizing the spot diameter to 0.03 mm and 0.02 mm exaggerates the power density

particularly at the lower values of f within the range from 20 to 25 kHz. At extreme power densities with the minimum spot diameter of 0.02 mm at high speeds of 440 mm/s and 500 mm/s, the OV between pulses was no longer exists which indicated by the negative sign. Compared with the low level of power density, as the graphs indicate the surface hardness of the alloy did not enhance at moderate and extreme power densities for the ranges 6.989 to 8.737 GW/cm² and 6.989 to 8.737 GW/cm² respectively. Both moderate and high levels share the same behavior as the low level but with significantly lower hardness values along the range as shown in Figure 4.

The results showed that the low levels band of power densities gave the best VHD as well better values for other set of parameters. Switching to the moderate level band of Pd causes a retreat in the values of microhardness keeping almost the same order for the effectiveness of Pd on microhardness. Utilizing the high band of power densities alters the order, where the proportionality becomes inverse. The higher power density yields the lowest sets for values of VHD, this may be regarded as the thermal effect of extreme values of power density that causes this reduction.

Although the frequency of pulses is considered when obtaining the pulse overlap and power density, the effect of it is somewhat unclear. The obtained experimental data for OV and f at the five low levels of employed Pd's in a two-dimensional array were represented. By taking the transpose of the built array the effective frequency on the microhardness at

different levels of average OV was obtained as shown in Figure 5. It is clear in all levels of power densities that the better microhardness of each group of samples was in the last quarter of 21 kHz to 22 kHz. This narrow band is classified as moderate f for the recommended employed range.

Figure 6 shows the effective f for moderate and high levels of Pd's. In moderate levels, working with higher frequencies yields better values of VHD while for high levels the worst values of microhardness are at the lowest value of f and can be enhanced by increasing it towards 25 kHz.

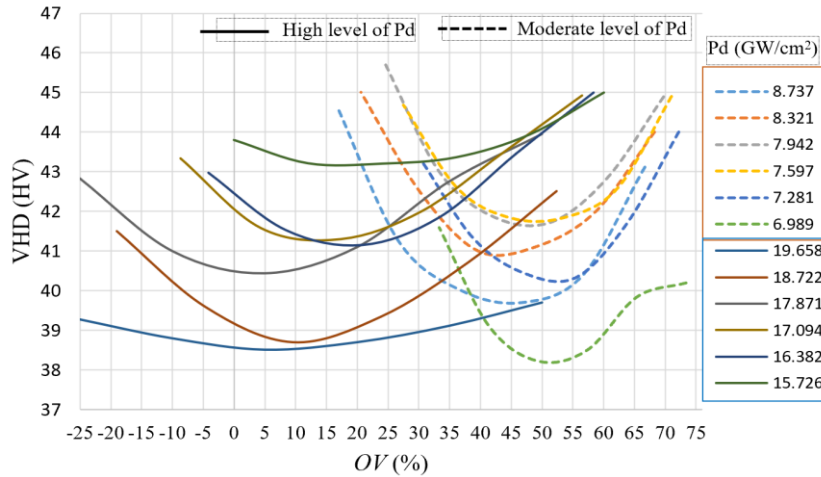


Figure 4. Effect of OV percentage on the surface VHD at two levels of Pd the high ranges from 15.762 to 19.658 GW/cm^2 and the moderate from 6.989 to 8.737 GW/cm^2 .

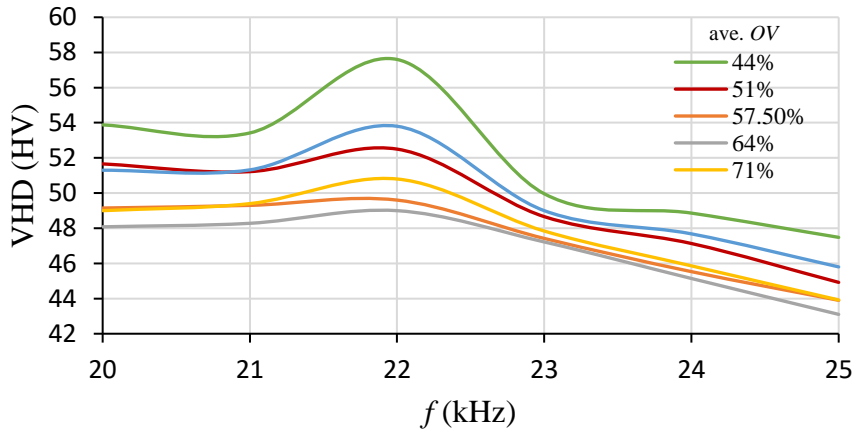


Figure 5. Effects of pulse frequency on the surface VHD at low level of OV percentages range from 44% to 77.5%

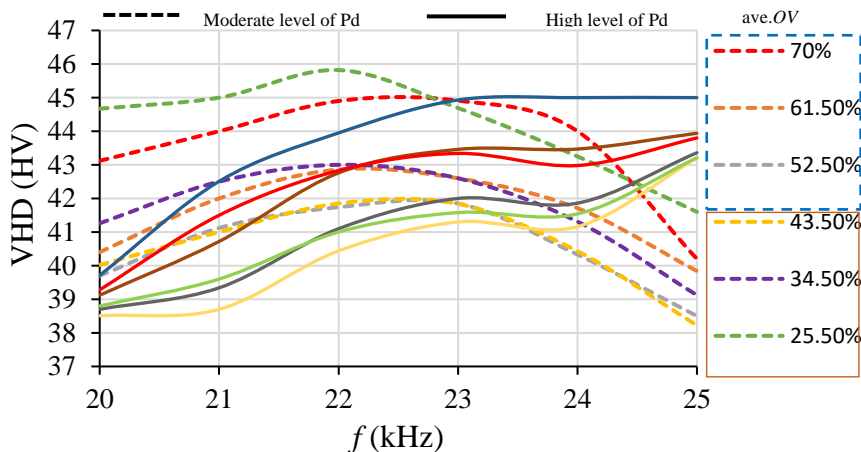


Figure 6. Effects of pulse frequency on the surface VHD at moderates and high levels of Pd's for a range of OV percentages range from -11.75% to 77%

3.2 Surface roughness

Ablation of the polymeric coat on the metal surface creates a plasma plume enclosed in the water layer of a certain pressure, which may alter the surface state. In addition, when the threshold of the applied laser exceeds the ablation of the polymeric coat the surface condition may be more changed due to localized melting, thermal defects or ablation of the base metal. The surface roughness (R_a) was inspected in two directions in each sample, parallel to the direction of laser scan vector (R_{ax}) and in the normal direction to the vector (R_{ay}).

Figure 7 shows the effect of OV on the R_{ax} and R_{ay} at all the low levels range of Pd (3.93 to 4.91 GW/cm^2) at which some better values of microhardness were obtained. along the x-axis it is clear that up to the range of 60% OV or even 64% OV in case of 4.91 GW/cm^2 , the R_{ax} is steady and have maximum value compared to its value when the OV increases drastically causing

the R_{ax} to decrease to lower level. At OV of 68% and up, the role of Pd in the reduction of R_{ax} to the minimum, of 0.5 μm , was clear where the curves shift down especially when the Pd at the maximum of 4.91 GW/cm^2 . Along the normal direction to the speed vector, the attitude is different, R_{ay} values had an inverse proportionality with increasing the OV percentage, and direct proportionality with the Pd values. The sensitivity of R_{ay} increases with the reduction of Pd. More OV to 80% and less Pd of 3.93 GW/cm^2 yield lower R_{ay} of 0.59 μm .

The mutual effect of f in kHz and OV percentage on the roughness is illustrated in Figure 8. Along the x-direction, R_{ax} tends to increase in an almost linear direct relationship with the f , but by switching to higher values of OV it tends to shift down toward finer roughness values. Along the y-direction, the relation between R_a and f is almost linear, and the relationship is converse. In addition, the R_{ay} curves move down as the OV percentage values increase.

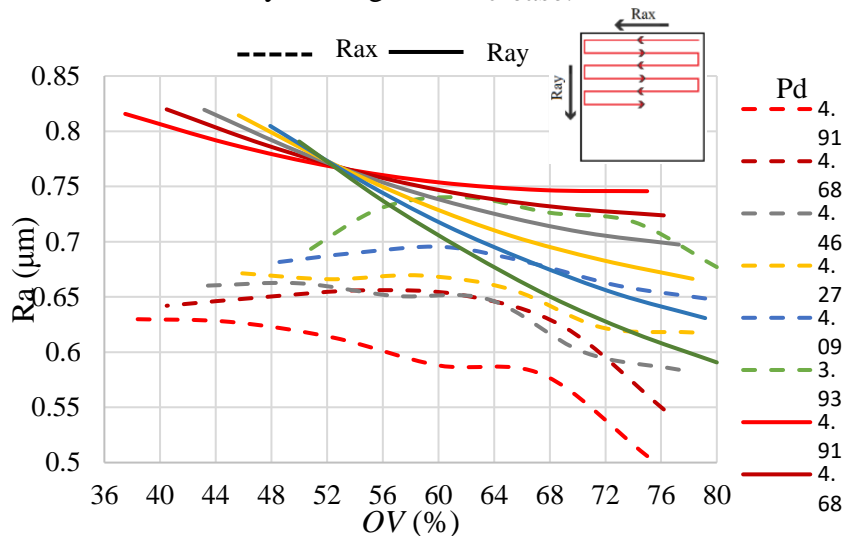


Figure 7. Surface roughness in the two directions x and y as a function of OV percentage at low levels of Pd ranges from 3.93 to 4.91 GW/cm^2

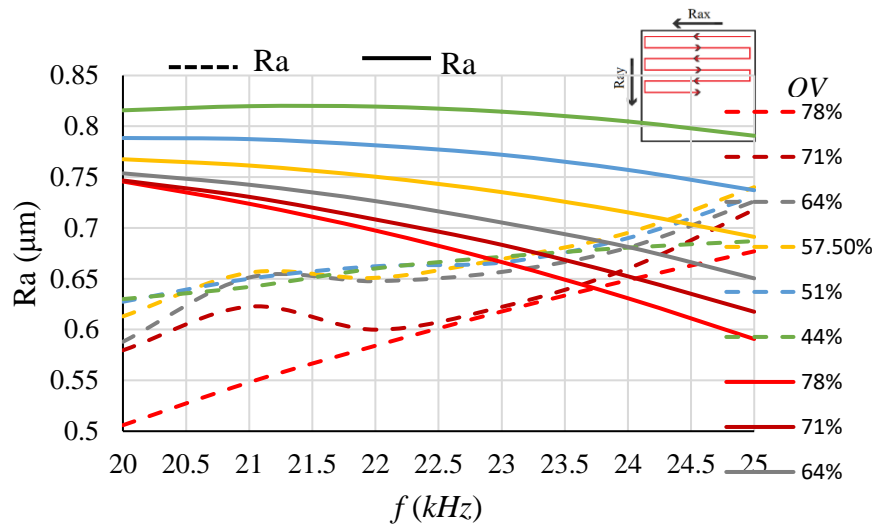


Figure 8. Surface roughness in the two directions x and y as a function of f at low level of OV percentages range from 44% to 78%

3.3 Scanning Electron Microscopy (SEM) Imaging

The high-resolution SEM images could be beneficial in giving evidence for the hardening nature whether it is cold through strain hardening or thermal processing. Figure 9 shows an image of the surface of the raw metal before processing with nanosecond laser (Z1) to be a reference for comparison with other images after processing. The corrugated texture of the surface results from the cold rolling of the metal to resize its thickness. Figure 10 illustrates the SEM images for some elected zones on the processed samples from Z2 to Z7 that were evaluated later through XRD analysis in the next section. Zone Z2 was processed with moderate level of Pd of 7.76 GW/cm^2 and OV of 48%, this caused defects due to ablation which can be recognized by some micro holes and grooves as well a reduction in the texture depth of the surface as shown in Figure 10a. Keeping the

same Pd with more reduction in the OV to 26% in zone Z3 did not support the hardness significantly. On the other hand, it makes the number of surface defects larger and deeper with less reduction in the surface texture compared with zone Z2 features as illustrated in Figure 10b.

Employing the maximum speed of 500 mm/s and minimum laser spot diameter of 0.02 mm in processing the zone Z4 has switched the Pd to an extreme value of 17.47 GW/cm^2 and yielded a negative OV of -11%. This resulted in a normal value of hardness of 40.3 HV, and high distortion in the surface of sample Z4 through localized deep melting, craters, and deep ablation as Figure 10c depicts. The previous images indicated that the samples Z2, Z3, and Z4 were subjected to cold working due to the compression of the plasma plume as well as softening due to thermal effects which were represented by the normal values of hardness, and skimming due to surface ablation.

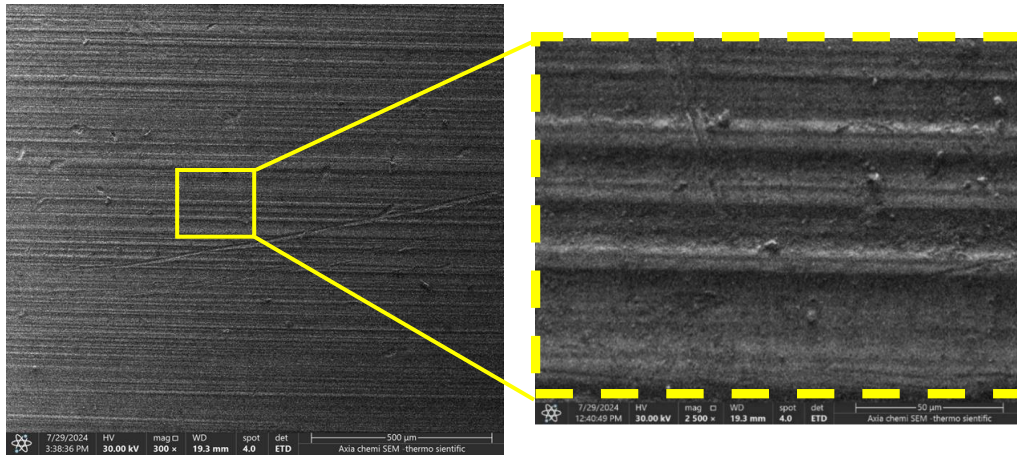
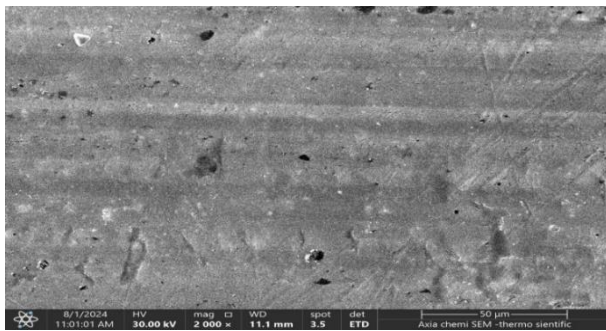
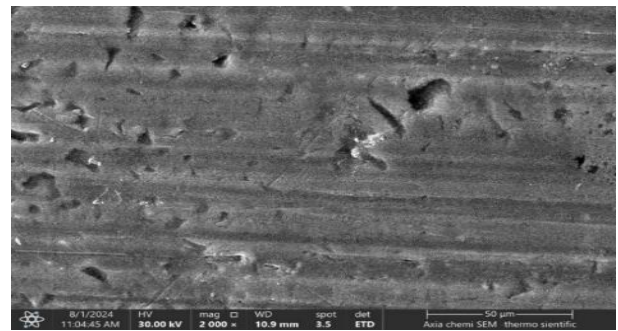


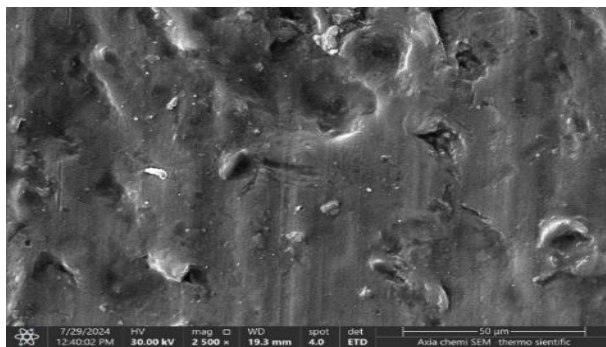
Figure 9. High resolution SEM image for the surface of the metal zone (Z1) before processing



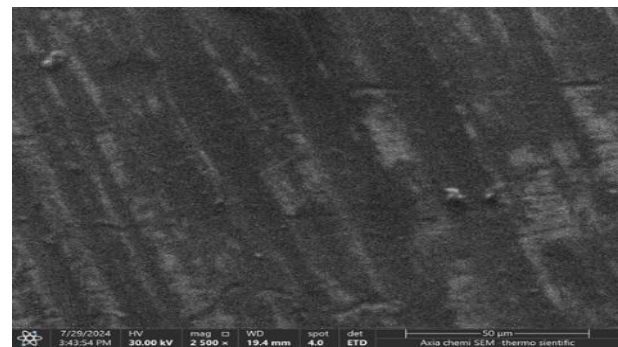
(a) Z2: Pd= 7.76 GW/cm², OV=48 %, VHD= 40.38 HV.



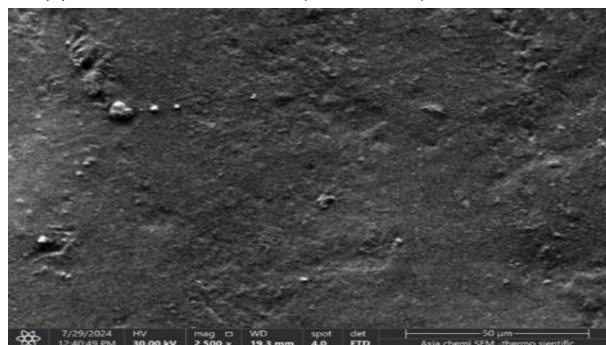
(b) Z3: Pd=7.76 GW/cm², OV= 26%, VHD= 45.21 HV.



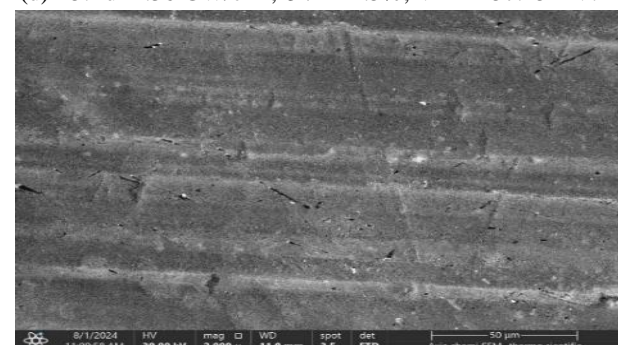
(c) Z4: Pd= 17.47 GW/cm², OV= -11%, VHD= 40.3 HV.



(d) Z5: Pd=4.36 GW/cm², OV= 44.5%, VHD= 57.25 HV.



(e) Z6: Pd=4.36 GW/cm², OV= 61%, VHD= 47.52 HV.



(f) Z7: Pd=7 GW/cm², OV= 33.5 %, VHD= 40.2 HV.

Figure 10. High resolution SEM images of some selected samples illustrate their hardened surfaces

Figure 10d revealed that the strain hardening process was conducted with sample Z5 by employing Pd of 4.36 GW/cm² and OV of 44.5%. This is indicated by the highest hardness of 57.25 HV, the absence of thermal defects, and the high matching of the surface texture with the raw sample. The most significant improvement in hardness was conducted at the low levels of power density and, OV percentage ranging from 43% to 58%. This recorded a maximum percentage increase in hardness of 80% compared with the raw metal hardness, which was associated with a clean, clear, and flawless surface, as well as non-thermal deformation.

Employing the same Pd of zone Z5 in zone Z6 with increasing the OV to 61% makes results in ablation of whole surface ablation and hardness degradation to 47.52 HV as shown in Figure 10e. Increasing Pd to 7 GW/cm² and reduction the OV to 33.5% degrades the surface quality and hardness to 40.2 HV in zone Z7 compared with zone Z5.

3.4 XRD Analysis

The X-ray diffraction (XRD) analysis reveals the existence of narrow diffraction peaks for the raw sample which shows some broadening for the hardened zones without yielding additional peaks. The narrow and sharp peaks indicates that the utilized alloy has well-ordered crystalline characteristics [38]. Aluminum 6061-O is an annealed soft and ductile alloy [39]. When the alloy is deformed with strain work, the diffraction peaks show some broadening indicates altering the crystalline sizes, microstrain, defects within the crystalline structure, and residual stresses [40]. The methodology put forth by Williamson and Hall was employed to ascertain the grain size and strain through the examination of peak width as a variable dependent on the diffraction peak position (2θ).

Table 3 tabulates the obtained data derived from the XRD analysis of the crystalline structure of one raw sample and six hardened zones and the feature of each zone based on SEM observations. Processing with nanosecond laser pulses on the upper surface of the optimum zone Z5 resulted in a discernible reduction in

grain size from 53.647 nm to noticeably lower values reaching 34.374 nm and the highest average strain of -903.81 $\mu\epsilon$. The reduction is achieved by using Pd of 4.36 GW/cm² and OV of 44.5%. In percentage talk, a reduction of 56% was observed in grain size when compared to the original raw sample and the number of dislocations density also increased by 378%. Increasing the OV from 44.5% to 61.11% in zone Z6 showed coarser grain size of 36.156, less numbers of dislocations of 0.6544 nm⁻² and average strain of -789.27 $\mu\epsilon$ yielding a noticeable reduction in hardness to 47.52 HV.

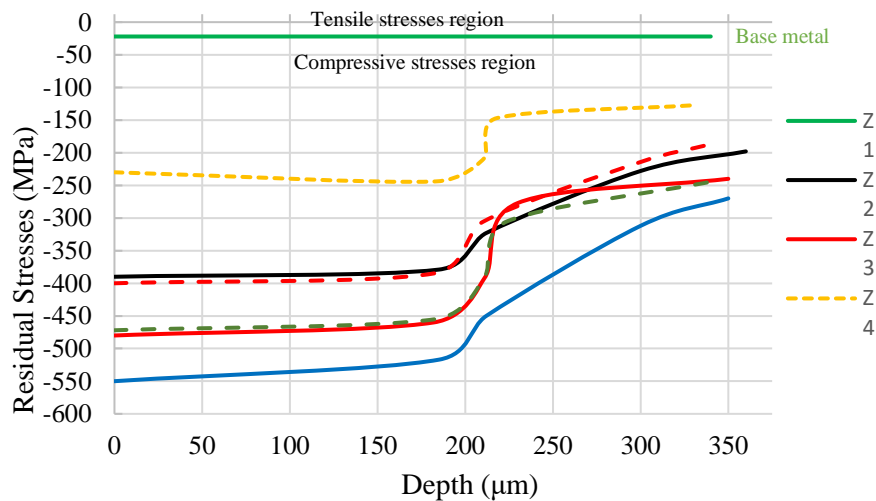
Despite Z4 being processed with extreme Pd of 17.47 GW/cm² it doesn't show a reduction in the grain size and average introduced strain. This lack of reduction is regarded to negative OV of -11% that was yielded from the high speed of 500 mm/s and minimum spot diameter of 0.02 mm. The hardened zone Z3 of 45.21 HV showed good reduction in the grain size and strain of 46.55nm and -850.82 $\mu\epsilon$ respectively. Z2 and Z7 samples show close results of reduction in grain size, strain and hardness.

The hardening process initiates cold working and plastic deformation within the treated zones, resulting in the formation of beneficial compressive residual stresses. The presence of induced residual stresses has been observed to enhance the hardness of materials and impede the initiation and propagation of micro-cracks [35,36]. Figure 11 depicts graphical representations of residual stresses as a function of depth for both the raw sample and several hardened zones with varying working parameters.

The graph illustrates that the raw sample exhibits a relatively low magnitude of residual compressive stresses, measuring at -22 MPa. In contrast to the latter, the hardened zones exhibited significant compressive residual stresses on the surface, with the minimum residual stress measuring -517 MPa at the surface and at zero depth. The maximum residual stress value of -127 was attained at a depth of 350 μm beneath the surface of the metal. The magnitude of residual stresses exhibits an ascending trend as one moves deeper below the surface, ultimately attaining a cumulative depth of 350 μm .

Table 3: Information extracted from the XRD test data for an untreated and hardened zones with the different process parameters. The grey shade refers to the best finding

Zone	Pd (GW/cm ²)	OV (%)	Ea (kJ/cm ²)	N (pulses/spot)	Hardness (HV)	Average grain size (nm)	Average dislocation (nm ⁻²)	Average strain (μϵ)	Surface features
Z1	The raw metal sample				32	53.647	0.1771	-426.6	Figure 9
Z2	7.76	48.15	0.953	1.93	40.5	48.106	0.4321	-664.71	Presence of little grooves & micro holes (Figure 10a)
Z3	7.76	26	0.667	1.35	45.21	37.622	0.7064	-805.82	More defects, holes &, ablated grooves (Figure 10b)
Z4	17.47	-11.11	1	0.9	40.5	52.692	0.3468	-427.28	Severe localized ablation, & recast materials (Figure 10c)
Z5	4.37	44.45	0.5	1.8	57.25	34.374	0.8462	-903.81	Ideal, clean & flawless (Figure 10d)
Z6	4.37	61.11	0.714	2.57	47.52	36.156	0.6544	-789.27	Fully ablated surface (Figure 10e)
Z7	6.99	33.34	0.667	1.5	40.19	46.553	0.4614	-628.32	Clean surface & little voids (Figure 10f)

**Figure 11.** Compressive residual stress is induced on the subsurface layers of the hardened zones at different sets of process parameters

4. Conclusions

The investigation introduces a good potential solution to increase the durability of mechanical components through enhancement of wear resistance, and fatigue strength. The following are the concluding remarks from the current study:

1. Manipulating a combination of the Pd and OV percentages results in different hardness values and could move the

hardening mode from strain hardening to a hot nature.

2. Employ low levels of Pd's of 4.27 to 4.91 GW/cm² and OV percentages ranging from 38 to 58% yield the better values of the hardness of 47 to 57.6 HV.
3. Transitioning from the low level of Pd to moderate and extreme levels within the ranges 6.989 to 8.737 GW/cm² and 6.989 to 8.737 GW/cm² respectively did not improve the hardness associated with thermal surface defects in most

cases, particularly with high OV percentages.

4. The choice of a suitable Pd and OV results in cold working deformation due to the effect of the high pressure of the plasma plume which induces residual stresses on the metal surface and beneath. At Pd of 4.46 GW/cm² and OV of 43%, strain hardening of 57.25 HV was achieved through cold working without thermal side effects on the metal surface.
5. Noticeable reduction in grain size from 53.647 nm to noticeably lower values reaching 34.374 nm and the highest average strain of -903.81 $\mu\epsilon$ is achieved when the strain hardening is applied at Pd of 4.36 GW/cm² and OV of 44.5 %.
6. The frequency of pulses has a significant effect on the hardness. In the low level of Pd, the frequency in the band of 21.5 to 22.5 kHz is recommended for processing while for moderate and high levels this narrow band changes and shows broadening.
7. At the low levels of Pd, a reduction of Rax roughness for the zones processed with OV of 68% and up, especially when the Pd was at the maximum of 4.91 GW/cm². Along the normal direction, Ray values had an inverse proportionality with increasing the OV and direct proportionality with the Pd values.

References

- [1] Y. Wang, Y. Zhu, S. Hou, H. Sun, and Y. Zhou, "Investigation on fatigue performance of cold expansion holes of 6061-T6 aluminum alloy," *Int. J. Fatigue*, vol. 95, pp. 216–228, Feb. 2017, doi: 10.1016/j.ijfatigue.2016.10.030.
- [2] A. G. Rao, M. Mohape, V. A. Katkar, D. S. Gowtam, V. P. Deshmukh, and A. K. Shah, "Fabrication and Characterization of Aluminum (6061)-Boron-Carbide Functionally Gradient Material," *Mater. Manuf. Process.*, vol. 25, no. 7, pp. 572–576, Jul. 2010, doi: 10.1080/10426910903180037.
- [3] Afaf M. Abd El-Hameed and Y. A. Abdel-Aziz, "Aluminium Alloys in Space Applications: A Short Report," *J. Adv. Res. Appl. Sci. Eng. Technol.*, vol. 22, no. 1, pp. 1–7, Jan. 2021, doi: 10.37934/araset.22.1.17.
- [4] Y. W. Tham, M. W. Fu, H. H. Hng, Q. X. Pei, and K. B. Lim, "Microstructure and Properties of Al-6061 Alloy by Equal Channel Angular Extrusion for 16 Passes," *Mater. Manuf. Process.*, vol. 22, no. 7–8, pp. 819–824, Sep. 2007, doi: 10.1080/10426910701446754.
- [5] I. Guzmán, E. Granda, J. Acevedo, A. Martínez, Y. Dávila, and R. Velázquez, "Comparative in Mechanical Behavior of 6061 Aluminum Alloy Welded by Pulsed GMAW with Different Filler Metals and Heat Treatments," *Materials (Basel)*, vol. 12, no. 24, p. 4157, Dec. 2019, doi: 10.3390/ma12244157.
- [6] A. H. Naronikar, H. N. A. Jamadagni, A. Simha, and B. Saikiran, "Optimizing the Heat Treatment Parameters of Al-6061 Required for Better Formability," *Mater. Today Proc.*, vol. 5, no. 11, pp. 24240–24247, 2018, doi: 10.1016/j.matpr.2018.10.219.
- [7] M. Benachour, N. Benachour, and M. Benguediab, "Effect of compressive residual stress generated by plastic preload on fatigue initiation of 6061 Al-alloy," *Procedia Struct. Integr.*, vol. 2, pp. 3090–3097, 2016, doi: 10.1016/j.prostr.2016.06.386.
- [8] A. Kaimkuriya, B. Sethuraman, and M. Gupta, "Effect of Physical Parameters on Fatigue Life of Materials and Alloys: A Critical Review," *Technologies*, vol. 12, no. 7, p. 100, Jul. 2024, doi: 10.3390/technologies12070100.
- [9] M. Karamimoghadam, M. Rezayat, M. Moradi, A. Mateo, and G. Casalino, "Laser Surface Transformation Hardening for Automotive Metals: Recent Progress," *Metals (Basel)*, vol. 14, no. 3, p. 339, Mar. 2024, doi: 10.3390/met14030339.
- [10] B. Peeters, O. Malek, S. Castagne, and B. Lauwers, "Selective laser hardening of injection mould components on multi-axis machining centers," *Procedia CIRP*, vol. 95, pp. 909–914, 2020, doi: 10.1016/j.procir.2020.01.154.
- [11] M. Rahman, J. Haider, and M. S. J. Hashmi, "Health and Safety Issues in Emerging Surface Engineering Techniques," in *Comprehensive Materials Processing*, Elsevier, 2014, pp. 35–47. doi: 10.1016/B978-0-08-096532-1.00806-2.
- [12] M. Dowling, A. R. Al-Hamaoy, and M. A. Obeidi, "Laser surface cladding of metal parts," *Results in Surfaces and Interfaces*, vol. 12, p. 100142, 2023, doi: https://doi.org/10.1016/j.rsufi.2023.100142.
- [13] A. Harnett, M. Ahmed Obeidi, I. U. Ahad, and A. R. Al-Hamaoy, "Comparing the surface hardness

- of mild steel processed with CO₂ and fibre lasers,” *Results Mater.*, vol. 18, p. 100400, 2023, doi: <https://doi.org/10.1016/j.rinma.2023.100400>.
- [14] J. Liu, C. Ye, and Y. Dong, “Recent development of thermally assisted surface hardening techniques: A review,” *Adv. Ind. Manuf. Eng.*, vol. 2, p. 100006, May 2021, doi: 10.1016/j.aime.2020.100006.
- [15] A. R. Alhamaoy, G. S. Sadiq, F. I. Hussein, and S. N. Ali, “The Cyclic Fatigue Behavior for 6061-T6 Al Alloy Shafts Processed by Laser Shock Peening,” *Mater. Sci. Forum*, vol. 1002, pp. 21–32, 2020, doi: 10.4028/www.scientific.net/MSF.1002.21.
- [16] A. Issa, F. I. Hussein Al-Najjar, A. Al-Hamaoy, and B. G. Rasheed, “Physical principles of laser–material interaction regimes for laser machining processes,” in *Laser Micro- and Nano-Scale Processing*, IOP Publishing, 2021. doi: 10.1088/978-0-7503-1683-5ch3.
- [17] M. R. Kasaai, V. Kacham, F. Theberge, and S. L. Chin, “The interaction of femtosecond and nanosecond laser pulses with the surface of glass,” *J. Non. Cryst. Solids*, vol. 319, no. 1–2, pp. 129–135, May 2003, doi: 10.1016/S0022-3093(02)01909-9.
- [18] J. Martan, J. Kunes, and N. Semmar, “Experimental mathematical model of nanosecond laser interaction with material,” *Appl. Surf. Sci.*, vol. 253, no. 7, pp. 3525–3532, Jan. 2007, doi: 10.1016/j.apsusc.2006.07.059.
- [19] R. Zhou, Z. Zhang, and M. Hong, “The art of laser ablation in aeroengine: The crown jewel of modern industry,” *J. Appl. Phys.*, vol. 127, no. 8, Feb. 2020, doi: 10.1063/1.5134813.
- [20] L. Gao, C. Liu, J. Liu, T. Yang, Y. Jin, and D. Sun, “Hole formation mechanisms in double-sided laser drilling of Ti6Al4V-C/SiC stacked materials,” *J. Mater. Process. Technol.*, vol. 325, p. 118307, Apr. 2024, doi: 10.1016/j.jmatprotec.2024.118307.
- [21] Z. Liao *et al.*, “Surface integrity in metal machining - Part I: Fundamentals of surface characteristics and formation mechanisms,” *Int. J. Mach. Tools Manuf.*, vol. 162, p. 103687, Mar. 2021, doi: 10.1016/j.ijmachtools.2020.103687.
- [22] A. M. Khudhair and F. I. Hussein, “High Speed Shock Peening by Fiber Laser for Al Alloy 6061-T6 Thin Sheets,” *J. Mater. Eng. Perform.*, vol. 31, no. 10, pp. 8585–8595, Oct. 2022, doi: 10.1007/s11665-022-07133-4.
- [23] S. Sathyajith and S. Kalainathan, “Effect of laser shot peening on precipitation hardened aluminum alloy 6061-T6 using low energy laser,” *Opt. Lasers Eng.*, vol. 50, no. 3, pp. 345–348, 2012, doi: 10.1016/j.optlaseng.2011.11.002.
- [24] O. Netprasert, V. Tangwarodomnukun, and C. Dumkum, “Surface Hardening of AISI 420 Stainless Steel by Using a Nanosecond Pulse Laser,” *Mater. Sci. Forum*, vol. 911, pp. 44–48, Jan. 2018, doi: 10.4028/www.scientific.net/MSF.911.44.
- [25] M. Ezzat, M. A. El-Waily, M. Abdel-Rahman, and Y. Ismail, “Treatment of Aluminum Alloys Surface by Nanosecond Laser,” *Surf. Rev. Lett.*, vol. 25, no. 04, p. 1850079, Jun. 2018, doi: 10.1142/S0218625X18500798.
- [26] A. M. Mostafa, M. F. Hameed, and S. S. Obayya, “Effect of laser shock peening on the hardness of AL-7075 alloy,” *J. King Saud Univ. - Sci.*, vol. 31, no. 4, pp. 472–478, Oct. 2019, doi: 10.1016/j.jksus.2017.07.012.
- [27] A. Kadhim, E. T. Salim, S. M. Fayadh, A. A. Al-Amiery, A. A. H. Kadhum, and A. B. Mohamad, “Effect of Multipath Laser Shock Processing on Microhardness, Surface Roughness, and Wear Resistance of 2024-T3 Al Alloy,” *Sci. World J.*, vol. 2014, pp. 1–6, 2014, doi: 10.1155/2014/490951.
- [28] C. Y. Ho, J. M. Holt, and H. Mindlin, *Structural Alloys Handbook: 1996 Edition; Incorporating Supplements Thought 1995*, no. v. 2. Cindas/Purdue Univ., 1997.
- [29] F. I. Hussein Al-Najjar, A. Al-Hamaoy, B. G. Rasheed, and A. Issa, “Effective working parameters of laser micro-/nano-machining,” in *Laser Micro- and Nano-Scale Processing*, IOP Publishing, 2021, pp. 44–66. doi: 10.1088/978-0-7503-1683-5ch4.
- [30] M. Rabiei, A. Palevicius, A. Monshi, S. Nasiri, A. Vilkauskas, and G. Janusas, “Comparing methods for calculating nano crystal size of natural hydroxyapatite using X-ray diffraction,” *Nanomaterials*, vol. 10, no. 9, pp. 1–21, 2020, doi: 10.3390/nano10091627.
- [31] M. Kawsar, M. S. Hossain, N. M. Bahadur, and S. Ahmed, “Synthesis of nano-crystallite hydroxyapatites in different media and a comparative study for estimation of crystallite size using Scherrer method, Halder-Wagner method size-strain plot, and Williamson-Hall model,” *Heliyon*, vol. 10, no. 3, p. e25347, 2024, doi: 10.1016/j.heliyon.2024.e25347.
- [32] A. Salimianrizi, E. Foroozmehr, M. Badrossamay, and H. Farrokhpour, “Effect of Laser Shock Peening on surface properties and residual stress of Al6061-T6,” *Opt. Lasers Eng.*, vol. 77, pp. 112–117, 2016, doi: 10.1016/j.optlaseng.2015.08.001.
- [33] Y.-F. Tzeng, “Process Characterisation of Pulsed

- Nd:YAG Laser Seam Welding,” *Int. J. Adv. Manuf. Technol.*, vol. 16, no. 1, pp. 10–18, Jan. 2000, doi: 10.1007/PL00013126.
- [34] P.-R. Jang, C.-G. Kim, G.-P. Han, M.-C. Ko, U.-C. Kim, and H.-S. Kim, “Influence of laser spot scanning speed on micro-polishing of metallic surface using UV nanosecond pulse laser,” *Int. J. Adv. Manuf. Technol.*, vol. 103, no. 1–4, pp. 423–431, Jul. 2019, doi: 10.1007/s00170-019-03559-8.
- [35] A. Gujba and M. Medraj, “Laser Peening Process and Its Impact on Materials Properties in Comparison with Shot Peening and Ultrasonic Impact Peening,” *Materials (Basel)*, vol. 7, no. 12, pp. 7925–7974, Dec. 2014, doi: 10.3390/ma7127925.
- [36] S. B. Puplampu, A. Siriruk, A. Sharma, and D. Penumadu, “Multiaxial deformation behavior of aluminum alloy 6061 subjected to fire damage,” *Mech. Mater.*, vol. 159, p. 103885, Aug. 2021, doi: 10.1016/j.mechmat.2021.103885.
- [37] Y. G. Ko and K. Hamad, “Annealing Behavior of 6061 Al Alloy Subjected to Differential Speed Rolling Deformation,” *Metals (Basel)*, vol. 7, no. 11, p. 494, Nov. 2017, doi: 10.3390/met7110494.
- [38] F. Ghahramanifard, A. Rouhollahi, and O. Fazlollahzadeh, “Electrodeposition of Cu-doped p-type ZnO nanorods; effect of Cu doping on structural, optical and photoelectrocatalytic property of ZnO nanostructure,” *Superlattices Microstruct.*, vol. 114, no. May 2018, pp. 1–14, 2018, doi: 10.1016/j.spmi.2017.07.019.
- [39] ASM Handbook Committee, Ed., “Heat Treating of Aluminum Alloys,” in *ASM Handbook, Volume 4: Heat Treating*, www.asminternational.org, 1991, pp. 841–879. doi: 10.1361/asmhba0001205.
- [40] B. D. C. and S. R. Stock, *Elements of X-Ray Diffraction*, 3rd Editio. Pearson Education Limited, 2014.
- [41] L. Doremus, J. Cormier, P. Villechaise, G. Henaff, Y. Nadot, and S. Pierret, “Influence of residual stresses on the fatigue crack growth from surface anomalies in a nickel-based superalloy,” *Mater. Sci. Eng. A*, vol. 644, pp. 234–246, Sep. 2015, doi: 10.1016/j.msea.2015.07.077.
- [42] Z. S. Ma, Y. C. Zhou, S. G. Long, and C. Lu, “Residual stress effect on hardness and yield strength of Ni thin film,” *Surf. Coatings Technol.*, vol. 207, pp. 305–309, Aug. 2012, doi: 10.1016/j.surfcoat.2012.07.002.